AUTHOR QUERY FORM

Dear Author,

Below are the queries associated with your article. Please answer all of these queries before sending the proof back to AIP.

Article checklist: In order to ensure greater accuracy, please check the following and make all necessary corrections before returning your proof.
1. Is the title of your article accurate and spelled correctly?
2. Please check affiliations including spelling, completeness, and correct linking to authors.
3. Did you remember to include acknowledgment of funding, if required, and is it accurate?

Location in article	Query/Remark: click on the Q link to navigate to the appropriate spot in the proof. There, insert your comments as a PDF annotation.
Q1	Please check that the author names are in the proper order and spelled correctly. Also, please ensure that each author's given and surnames have been correctly identified (given names are highlighted in red and surnames appear in blue).
Q2	In accordance with standard AIP journal style, we have inserted the corresponding author email address from readme.xml. Please check.
Q3	We have reworded the sentence beginning "One first major hurdle is..." for clarity. Please check that your meaning is preserved.
Q4	We have reworded the sentence beginning "Finally, after placing the chips on..." for clarity. Please check that your meaning is preserved.
Q5	We have reworded the sentence beginning "Images acquired from these..." for clarity. Please check that your meaning is preserved.
Q6	We have reworded the sentence beginning "With proper UV exposure..." for clarity. Please check that your meaning is preserved.
Q7	Please provide volume number in Refs. 36 and 49.
Q8	Please confirm the page number and year of publication in Ref. 36, as we have inserted the required information.
Q9	Please update Ref. 44 with journal name, volume number, page number, and year if published. If not yet published, please provide the article title and, if available, the journal title. If the article is an "early" or "advance" view published online by a journal before assignment to a volume and issue, please provide a DOI if available.
Q10	Please confirm the page number in Ref. 49, as we have inserted the required information.

Continued on next page.

Continued from previous page.

Please confirm ORCIDs are accurate. If you wish to add an ORCID for any author that does not have one, you may do so now. For more information on ORCID, see https://orcid.org/.

Dinesh Patel –
Martina Marzano – 0000-0001-5288-3093
Chieh-I Liu –
Heather M. Hill –
Mattias Kruskopf – 0000-0003-2846-3157
Hanbyul Jin – 0000-0001-9295-444X
Jiuning Hu –
David B. Newell –
Chi-Te Liang – 0000-0003-4435-5949
Randolph Elmquist – 0000-0001-9041-7966
Albert F. Rigosi – 0000-0002-8189-3829

Thank you for your assistance.

Accessing ratios of quantized resistances in graphene *p–n* junction devices using multiple terminals

View Online   Export Citation   CrossMark

Dinesh Patel,[1,2] **Martina Marzano,**[1,3,4] (iD) **Chieh-I Liu,**[1] **Heather M. Hill,**[1] **Mattias Kruskopf,**[1,5] (iD)
Hanbyul Jin,[1,5] (iD) **Jiuning Hu,**[1,5] **David B. Newell,**[1] **Chi-Te Liang,**[2] (iD)
Randolph Elmquist,[1] (iD) **and Albert F. Rigosi**[1,a)] (iD)

AFFILIATIONS

[1] Physical Measurement Laboratory, National Institute of Standards and Technology (NIST), Gaithersburg,
Maryland 20899-8171, USA
[2] Department of Physics, National Taiwan University, Taipei 10617, Taiwan
[3] Department of Electronics and Telecommunications, Politecnico di Torino, Torino 10129, Italy
[4] Istituto Nazionale di Ricerca Metrologica, Torino 10135, Italy
[5] Joint Quantum Institute, University of Maryland, College Park, Maryland 20742, USA

[a)] Author to whom correspondence should be addressed: albert.rigosi@nist.gov

ABSTRACT

The utilization of multiple current terminals on millimeter-scale graphene *p–n* junction devices has enabled the measurement of many atypical, fractional multiples of the quantized Hall resistance at the $\nu = 2$ plateau ($R_H \approx 12\,906\ \Omega$). These fractions take the form $\frac{a}{b}R_H$ and can be determined both analytically and by simulations. These experiments validate the use of either the LTspice circuit simulator or the analytical framework recently presented in similar work. Furthermore, the production of several devices with large-scale junctions substantiates the approach of using simple ultraviolet lithography to obtain junctions of sufficient sharpness.

Graphene, composed of carbon atoms arranged in a two-dimensional honeycomb lattice, has been extensively studied for more than a decade, in part because of its excellent optical, mechanical, and electrical transport properties.[1–4] The quantum Hall effect (QHE) in graphene gives resistance values at $\frac{1}{(4n+2)}\frac{h}{e^2}$, where *n* is an integer, *h* is the Planck constant, and *e* is the elementary charge. Graphene *p–n* junctions (*pn*Js), which are suitable for one to explore transport in the QHE,[5–18] enable one to access various multiples and fractions of the von Klitzing constant. These types of graphene devices also have additional applications in electron optics,[19–22] photodetection,[23–27] and quantum Hall resistance standards.[28–38]

For clarity, a *pn*J device contains some form of interface at which a positively doped and a negatively doped region meet. For graphene, whose Fermi level can be electrically or chemically modulated, such an interface can be effectively one-dimensional, allowing edge state electrons to tunnel from one region to the other. This behavior results in the observation of quantized longitudinal resistances due to the presence of the junction. Typically, these devices are of sub-millimeter sizes due to constraints on top-gating. One motivation for pursuing large-scale *pn*J devices is to determine the feasibility of using quantum transport across the junctions to access different quantized values of resistance, as shown in previous studies.[39–41] One first major hurdle is to fabricate large-scale devices without the need for top-gating, since such techniques become more complicated as the device incorporates more elements. Although extensive analyses exist on Landauer–Büttiker edge state equilibration,[5–8,42–46] creating a *pn*J device capable of accessing different plateaus with top gates is a difficult task. Instead, one approach to accessing different quantized values is to incorporate multiple

current terminals, which opens the parameter space within which *pn*J devices are able to be operated.

For millimeter-scale device fabrication, epitaxial graphene (EG) is grown to accommodate device size, but the issue of processing the correspondingly large *pn*Js was not trivial, as shown in previous work.[47] This work elaborates on further efforts involving the use of standard ultraviolet photolithography (UVP) and ZEP520A to build *pn*Js having widths smaller than 200 nm. Devices were verified via quantum Hall transport measurements and LTspice current simulations,[48] and multiple current terminals and configurations were used to test the viability of the simulations as well as the quality of the devices. Furthermore, recently reported analytical methods were also used to predict atypical fractions of the quantized Hall resistance, R_H, that would become experimentally accessible depending on the configuration of the current terminals.[49] These experiments also serve as supporting evidence on the validity of those analytical methods, which provide easily implementable algorithms for determining effective quantized resistances in complicated *pn*J circuits.

Simulations for the *pn*J devices were performed with the analog electronic circuit simulator LTspice in an identical manner as demonstrated for similar devices in other works.[47,49–51] The circuit uses both *p*-type and *n*-type *k*-terminal quantum Hall elements, designated as either having ideal counterclockwise (CCW) or clockwise (CW) edge state current flow. EG on SiC was fabricated into *pn*J devices after the growth at a temperature of 1900 °C. First, chips were diced from 4*H*-SiC(0001) wafers (CREE)[48] and chemically cleaned with a 5:1 diluted solution of hydrofluoric acid and deionized water. Just prior to growth, chips were processed with AZ5214E to utilize polymer-assisted sublimation.[52] Finally, after placing the chips on a polished graphite substrate (SPI Glas 22)[50] silicon-face down, the growth occurred under an ambient argon environment at 1900 °C with a graphite-lined resistive-element furnace (Materials Research Furnaces, Inc.).[48] The corresponding heating and cooling rates of the furnace were about 1.5 °C/s.

Once grown, EG was assessed with confocal laser scanning, optical, and atomic force microscopy (AFM).[53] Images acquired from these techniques are provided in Fig. 1, which confirmed that homogeneous monolayer EG had successfully covered millimeter-scale areas (see the supplementary material for additional AFM images). Next, using Pd and Au as protective layers against organic contamination, photolithographic processes were performed, details of which may be found in other works.[31,47] Once each Hall bar device was completed, it underwent Cr(CO)$_3$ functionalization to reduce
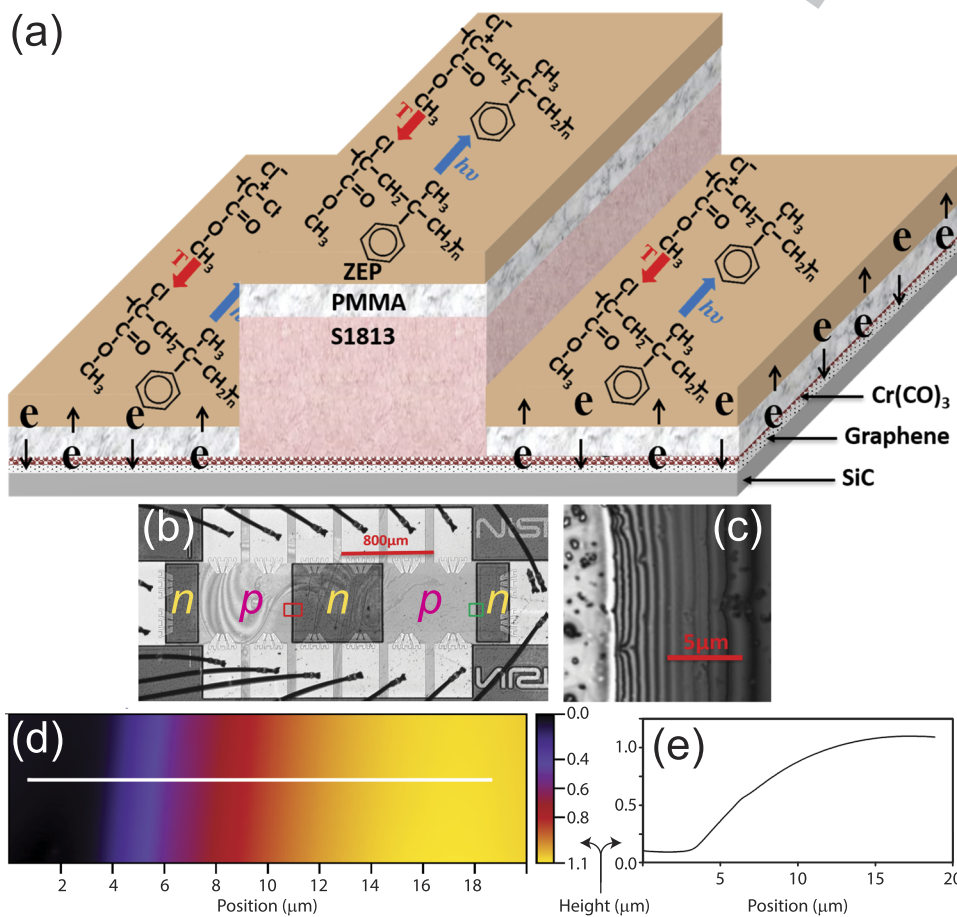
FIG. 1. (a) An illustration of the surface of an EG *pn*J device. The photoresist S1813 was deposited and lithographically processed on specific regions where *n*-type doping was preferred. The molecule in ZEP520A is shown to clarify the electron acceptor as the photoresist is exposed to ultraviolet light. Cr(CO)$_3$ was used to stabilize the electron density. (b) A confocal microscope image acquired for the full device after wire bonding, with the darker region indicating the desired *n*-type regions. (c) A magnification of the small green box in (b) for a scale of the order of 5 μm. Oxidized residue from the Cr(CO)$_3$ deposition takes the form of visible black specs. (d) and (e) show both the two-dimensional and one-dimensional height profiles, respectively, with the one-dimensional profile represented as a white line in (d) and the two-dimensional profile acquired within the red box in (b).

123　the electron density to approximately 10^{10} cm^{-2}.[54–58] The major final
124　steps included the deposition of S1813 photoresist as a spacer layer
125　for intended *n*-type regions, PMMA/MMA photoresist as an addi-
126　tional spacer, and ZEP520A as a photoactive layer, as described in
127　the literature.[47,59] Uniformity is also verified with Raman spectra (see
128　the supplementary material).

129　　　Although AFM images suggest a sloped S1813 spacer layer,
130　preservation of the *n*-type regions can still be accomplished with
131　thicknesses of the order of 100 nm.[49] Furthermore, the upper bound
132　of the junction width resulting from these photolithographic pro-
133　cesses was measured to be approximately 200 nm in another work,
134　rendering them of sufficient sharpness to accommodate edge-state
135　propagation.[49] Ultraviolet (UV) light, with a wavelength of 254 nm,
136　was used to realize *p*-type doping in regions without S1813. The lon-
137　gitudinal resistivity was monitored during periods of UV exposure,
138　and additional information and data on this process are found in the
139　supplementary material.

140　　　Completed four-junction devices, like the one shown in
141　Fig. 1(c), were measured with the traditional methods to verify
142　that regions exhibited resistance quantization. This type of device
143　is shown in Fig. 2(a). Electrical contact pads are numbered based on
144　the measurement system used to provide the corresponding mea-
145　surements in (b) and (c). Traditional longitudinal and Hall mea-
146　surements were acquired at 1.6 K and ±9 T, with the results shown
147　in Fig. 2(b) as black and red curves, respectively. With proper UV

148　exposure, regions without the S1813 spacer layer are subject to *p*
149　doping, and after sufficient exposure time, they become set as *p*-type
150　regions.

151　　　The resulting *pn*Js were found to be of sufficient narrowness
152　to accommodate dissipationless edge-state propagation.[47] However,
153　to further verify that the entire device was functional, voltage mea-
154　surements were performed along the length of the device, bearing
155　in mind the formation of the device's so-called hot spots, as shown
156　pictorially in Ref. 40. In Fig. 2(c), the plotted resistances further sup-
157　port the idea that millimeter-scale *pn*Js can be successfully fabricated
158　with standard UV lithography.

159　　　A recent formulation for using multiple terminals on a *pn*J
160　device as the only resistive elements of a circuit has established a
161　mathematical way of predicting the effective quantized resistance of
162　that circuit.[49] Essentially, a single current source can inject current
163　into an arbitrary number of terminals—likewise for the drain port of
164　the current source. The voltage difference of the whole circuit, and
165　by extension the effective quantized resistance $R_{eff} = q_{N-1}R_H$, can
166　then be measured between just after the current source starts and just
167　before the drain of the current source terminates. The coefficient of
168　effective resistance (CER) is labeled *q* and represents a device config-
169　uration containing *N* total terminals that are used (either as a source
170　or as a drain).

171　　　Eight different configurations were measured, and their effec-
172　tive circuit resistances are plotted in Fig. 3. Furthermore, two meth-
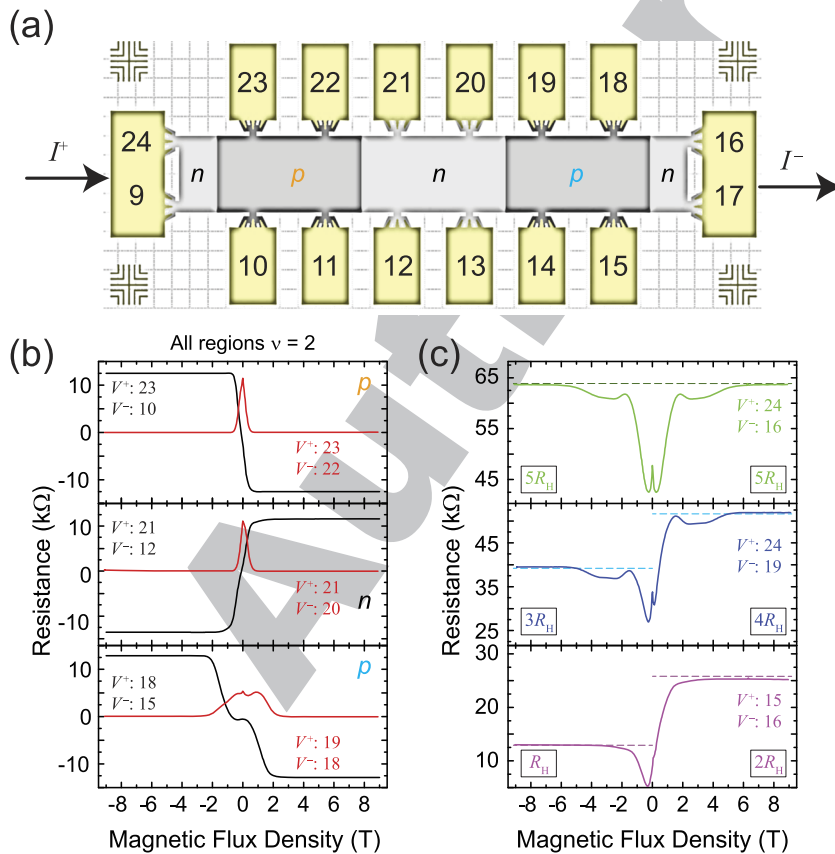
FIG. 2. (a) A four-junction device illustration with numbers corresponding to wired connections on a 32-pin leadless chip carrier, with the electron flow entering from the right-side contact (drain) and with the source on the left side. A current of 1 μA was applied for all measurements. Darker and lighter gray colors indicate *p*-type and *n*-type regions, respectively. The three middle regions are tested to check traditional Hall resistance curves, with orange and cyan *p* labels matching those seen in (b). (b) The longitudinal and Hall resistances were measured from 9 T to −9 T at 1.6 K and are represented by red and black curves, respectively. Pin labels are also provided. (c) Integer multiples of R_H (from 1 to 5) were measured across varying lengths of the device to ensure device functionality. Dotted lines are provided as a visual guide to compare exact quantized values. All regions were on the $\nu = 2$ plateau.
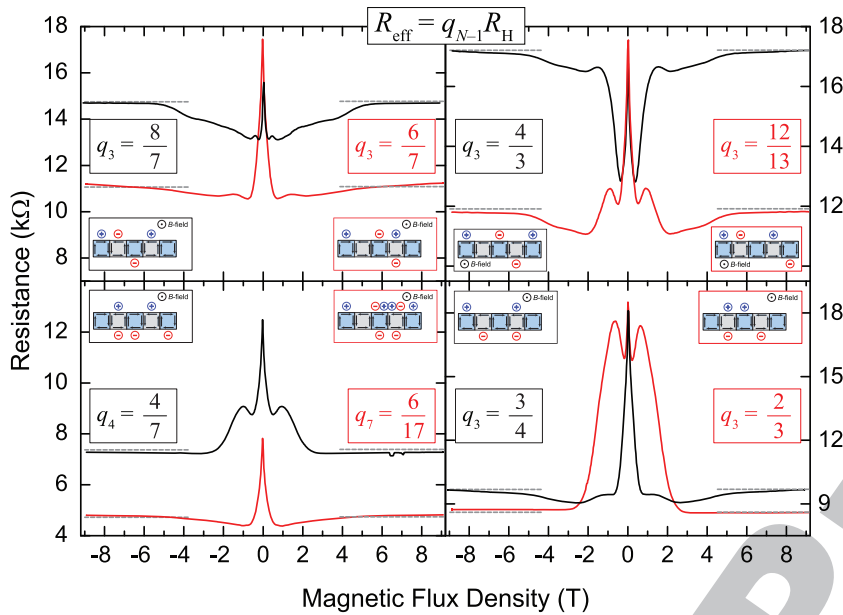
FIG. 3. Multiple-terminal configurations have been measured and their effective circuit resistances are plotted in the four panels. Three of the four panels contain four-terminal configurations (two sources and two drains), whereas the panel on the lower left corner uses a five-terminal and an eight-terminal configuration. The latter panel, when compared with the calculated and simulated value in dotted gray lines, provides some evidence that the CER formulation is valid for larger numbers of used terminals. All panels contain the calculated and simulated value in dotted gray lines (valid for sufficiently high magnetic flux density), and for all cases, the calculated and simulated results agree with each other. The insets of each panel have colored perimeters corresponding to the curve of the same color and illustrate the four-junction device and its edge-state current flow abstractly. The blue plus and red minus signs indicate source and drain terminals, respectively.
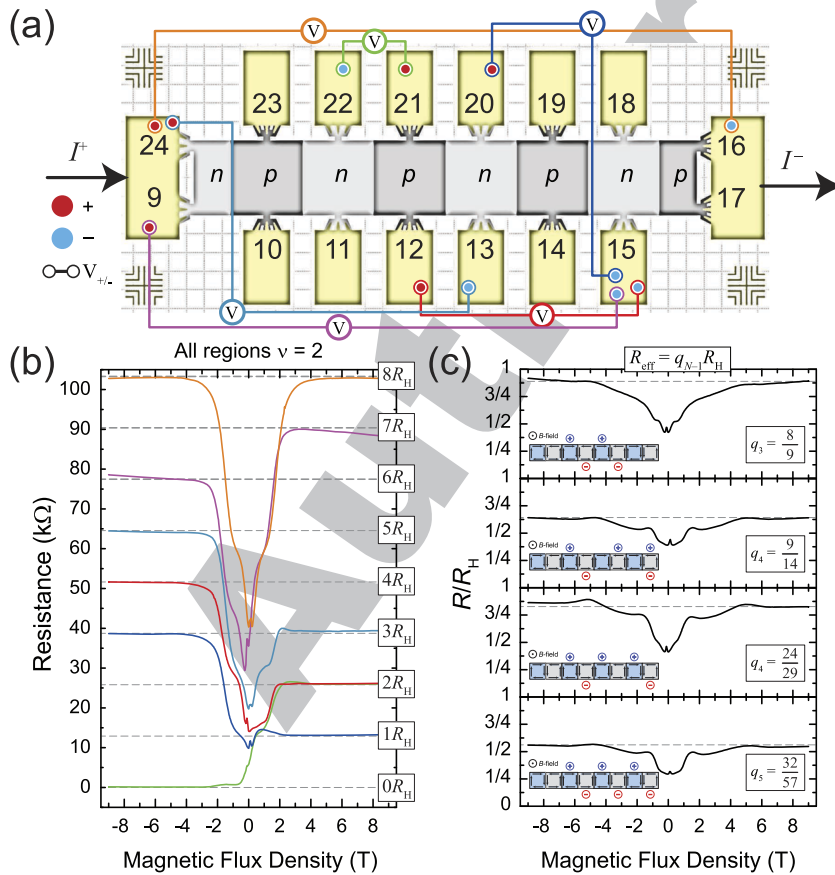
FIG. 4. (a) A seven-junction device illustration with numbers corresponding to the same measurement system is shown using a measurement current of 1 μA. Darker and lighter gray colors indicate p-type and n-type regions, respectively. Each measurement pair is color-coded for easy comparison to its corresponding data. (b) The resistance is plotted for each of the voltage measurement pairs in (a) with the same color-coding used to match the illustration. The dotted gray lines represent the exact values of the multiples of R_H. All regions were on the $\nu = 2$ plateau. (c) Several new configurations were measured and compared with both simulations and the CER formulation, with the latter two in exact agreement. Thus, both theoretical values are represented by the same gray dotted line in each of the four panels. On the bottom left of each graph panel, the illustrated device is shown with the corresponding locations of sources (blue plus symbol) and drains (red minus symbol) along the device. Voltages were measured from the point before the sources split to the point after the drains rejoin, yielding the CERs of each configuration.

ods were used to predict the expected CERs of the circuit—the LTspice simulator and the CER formulation. Both methods agreed exactly and are plotted as gray dotted lines for each of the eight configurations. The crucial formula used to mathematically predict the expected CERs[49] is as follows:

$$q_{N-1}(n_{N-1}) = \frac{q_{N-2}(n_{N-1}+1)}{n_{N-1}+\frac{q_{N-2}}{q_{N-1}^{(0)}}}. \tag{1}$$

The CERs calculated in Fig. 3 include the following: $\{\frac{6}{7}, \frac{8}{7}, \frac{12}{13}, \frac{4}{3}, \frac{6}{17}, \frac{4}{7}, \frac{3}{4}, \frac{2}{3}\}$. Details on how to proceed with the calculation are well-documented in Ref. 49, and additional examples for some of the configurations in this manuscript are found in the supplementary material.

To demonstrate how increasingly complex calculations can yield atypical CERs, devices containing seven pnJs were fabricated as shown in Fig. 4(a). Although even more pnJs can be placed along the 2 mm length of the device, their number was limited by the preference of accessing each region with an electrical contact for proof of concept. Figure 4(a) shows voltage leads of varying color that were used for determining the resistance curves and by extension the CERs [Fig. 4(b)].

Sufficient quantization was seen for the more traditional cases of measuring the resistance across parts of the device while the source and drain are at the farthest terminals. All integer multiples of R_H between 1 and 8 were accessible in this characterization, warranting further measurements with multiple terminals. In Fig. 4(c), four configurations were measured using different numbers of total terminals. The top panel, using four terminals as illustrated in the inset, yielded data that were then compared to the predicted CER of $q_3 = \frac{8}{9}$. The two middle panels used five terminals and were compared with their corresponding predicted values of $q_4 = \frac{9}{14}$ and $q_4 = \frac{24}{29}$. In the bottom panel, the six-terminal configuration was measured and compared with its corresponding prediction of $q_5 = \frac{32}{57}$. For the sake of clarity and as an additional tutorial, this fourth case is calculated in more detail in the supplementary material. Overall, such devices and their CERs can be measured for many configurations of similar or greater complexity. Moreover, desired, user-specific CERs can be reversed engineered into a corresponding configuration.

In conclusion, this work pursued further efforts involving pnJ devices fabricated from EG on SiC with junction widths sufficiently narrow to observe usual edge-state propagation. By configuring an experimental setup to include multiple sources and drains, various atypical quantized resistances became accessible and matched predicted values based on LTspice simulations. Additionally, recently reported analytical methods were also used to support the predicted values of the same atypical fractions of R_H. The results demonstrate that pnJs have the potential to bring scalable resistance values as well as reinforce the validity of the aforementioned CER formulation, which provides a simple algorithm for determining the effective quantized resistances in pnJ circuits.

See the supplementary material for the details on UV exposure and for additional calculations.

REFERENCES

[1] A. K. Geim and K. S. Novoselov, Nat. Mater. 6, 183 (2007).
[2] A. H. Castro Neto, F. Guinea, N. M. R. Peres, K. S. Novoselov, and A. K. Geim, Rev. Mod. Phys. 81, 109 (2009).
[3] K. S. Novoselov, V. I. Fal'ko, L. Colombo, P. R. Gellert, M. G. Schwab, and K. Kim, Nature 490, 192 (2012).
[4] S. Das Sarma, S. Adam, E. H. Hwang, and E. Rossi, Rev. Mod. Phys. 83, 407 (2011).
[5] J. R. Williams, L. DiCarlo, and C. M. Marcus, Science 317, 638 (2007).
[6] B. Huard, J. A. Sulpizio, N. Stander, K. Todd, B. Yang, and D. Goldhaber-Gordon, Phys. Rev. Lett. 98, 236803 (2007).
[7] B. Özyilmaz, P. Jarillo-Herrero, D. Efetov, D. A. Abanin, L. S. Levitov, and P. Kim, Phys. Rev. Lett. 99, 166804 (2007).
[8] N. N. Klimov, S. T. Le, J. Yan, P. Agnihotri, E. Comfort, J. U. Lee, D. B. Newell, and C. A. Richter, Phys. Rev. B 92, 241301 (2015).
[9] S. W. LaGasse and J. U. Lee, Phys. Rev. B 94, 165312 (2016).
[10] A. F. Young and P. Kim, Nat. Phys. 5, 222 (2009).
[11] J. R. Williams, T. Low, M. S. Lundstrom, and C. M. Marcus, Nat. Nanotechnol. 6, 222 (2011).
[12] H. Schmidt, J. C. Rode, D. Smirnov, and R. J. Haug, Phys. Rev. B 88, 075418 (2013).
[13] F. Amet, J. R. Williams, K. Watanabe, T. Taniguchi, and D. Goldhaber-Gordon, Phys. Rev. Lett. 112, 196601 (2014).
[14] T. Taychatanapat, J. Y. Tan, Y. Yeo, K. Watanabe, T. Taniguchi, and B. Özyilmaz, Nat. Commun. 6, 6093 (2015).
[15] P. Rickhaus, M. H. Liu, P. Makk, R. Maurand, S. Hess, S. Zihlmann, M. Weiss, K. Richter, and C. Schönenberger, Nano Lett. 15, 5819 (2015).
[16] N. Kumada, F. D. Parmentier, H. Hibino, D. C. Glattli, and P. Roulleau, Nat. Commun. 6, 8068 (2015).
[17] J. Lee, D. Wong, J. Velasco, Jr., J. F. Rodriguez-Nieva, S. Kahn, H.-Z. Tsai, T. Taniguchi, K. Watanabe, A. Zettl, F. Wang, L. S. Levitov, and M. F. Crommie, Nat. Phys. 12, 1032–1036 (2016).
[18] X. Gan, R.-J. Shiue, Y. Gao, I. Meric, T. F. Heinz, K. Shepard, J. Hone, S. Assefa, and D. Englund, Nat. Photonics 7, 883 (2013).
[19] Y. Zhao, J. Wyrick, F. D. Natterer, J. F. Rodriguez-Nieva, C. Lewandowski, K. Watanabe, T. Taniguchi, L. S. Levitov, N. B. Zhitenev, and J. A. Stroscio, Science 348, 672 (2015).
[20] S. Chen, Z. Han, M. M. Elahi, K. M. Masum Habib, L. Wang, B. Wen, Y. Gao, T. Taniguchi, K. Watanabe, J. Hone, A. W. Ghosh, and C. R. Dean, Science 353, 1522 (2016).
[21] M. M. Elahi, K. M. Masum Habib, K. Wang, G.-H. Lee, P. Kim, and A. W. Ghosh, Appl. Phys. Lett. 114, 013507 (2019).
[22] V. V. Cheianov, V. Fal'ko, and B. L. Altshuler, Science 315, 1252 (2007).
[23] F. Ghahari, D. Walkup, C. Gutiérrez, J. F. Rodriguez-Nieva, Y. Zhao, J. Wyrick, F. D. Natterer, W. G. Cullen, K. Watanabe, T. Taniguchi, L. S. Levitov, N. B. Zhitenev, and J. A. Stroscio, Science 356, 845 (2017).
[24] J. Fang, D. Wang, C. T. DeVault, T.-F. Chung, Y. P. Chen, A. Boltasseva, V. M. Shalaev, and A. V. Kildishev, Nano Lett. 17, 57 (2017).
[25] T. Mueller, F. Xia, and P. Avouris, Nat. Photonics 4, 297 (2010).
[26] S. Schuler, D. Schall, D. Neumaier, L. Dobusch, O. Bethge, B. Schwarz, M. Krall, and T. Mueller, Nano Lett. 16, 7107 (2016).
[27] F. Xia, T. Mueller, Y. Lin, A. Valdes-Garcia, and P. Avouris, Nat. Nanotechnol. 4, 839 (2009).
[28] A. F. Rigosi and R. E. Elmquist, Semicond. Sci. Technol. 34, 093004 (2019).
[29] T. J. B. M. Janssen, A. Tzalenchuk, R. Yakimova, S. Kubatkin, S. Lara-Avila, S. Kopylov, and V. I. Fal'ko, Phys. Rev. B 83, 233402 (2011).

[30] A. Tzalenchuk, S. Lara-Avila, A. Kalaboukhov, S. Paolillo, M. Syväjärvi, R. Yakimova, O. Kazakova, T. J. B. M. Janssen, V. Fal'ko, and S. Kubatkin, Nat. Nanotechnol. **5**, 186 (2010).

[31] A. F. Rigosi, C.-I. Liu, N. R. Glavin, Y. Yang, H. M. Hill, J. Hu, A. R. Hight Walker, C. A. Richter, R. E. Elmquist, and D. B. Newell, ACS Omega **2**, 2326 (2017).

[32] R. Ribeiro-Palau, F. Lafont, J. Brun-Picard, D. Kazazis, A. Michon, F. Cheynis, O. Couturaud, C. Consejo, B. Jouault, W. Poirier, and F. Schopfer, Nat. Nanotechnol. **10**, 965 (2015).

[33] A. F. Rigosi, N. R. Glavin, C.-I. Liu, Y. Yang, J. Obrzut, H. M. Hill, J. Hu, H.-Y. Lee, A. R. Hight Walker, C. A. Richter, R. E. Elmquist, and D. B. Newell, Small **13**, 1700452 (2017).

[34] Y. Fukuyama, R. E. Elmquist, L.-I. Huang, Y. Yang, F.-H. Liu, and N.-H. Kaneko, IEEE Trans. Instrum. Meas. **64**, 1451 (2015).

[35] A. F. Rigosi, A. R. Panna, S. U. Payagala, M. Kruskopf, M. E. Kraft, G. R. Jones, B.-Y. Wu, H.-Y. Lee, Y. Yang, J. Hu, D. G. Jarrett, D. B. Newell, and R. E. Elmquist, IEEE Trans. Instrum. Meas. **68**, 1870 (2019).

[36] T. Oe, A. F. Rigosi, M. Kruskopf, B.-Y. Wu, H.-Y. Lee, Y. Yang, R. E. Elmquist, N.-H. Kaneko, and D. G. Jarrett, IEEE Trans. Instrum. Meas. ∎, 1 (2019).

[37] M. Kruskopf, A. F. Rigosi, A. R. Panna, D. K. Patel, H. Jin, M. Marzano, M. Berilla, D. B. Newell, and R. E. Elmquist, IEEE Trans. Electron Devices **66**, 3973 (2019).

[38] M. Kruskopf, A. F. Rigosi, A. R. Panna, M. Marzano, D. K. Patel, H. Jin, D. B. Newell, and R. E. Elmquist, Metrologia **56**, 065002 (2019).

[39] J. Hu, A. F. Rigosi, J. U. Lee, H.-Y. Lee, Y. Yang, C.-I. Liu, R. E. Elmquist, and D. B. Newell, Phys. Rev. B **98**, 045412 (2018).

[40] M. Woszczyna, M. Friedmann, T. Dziomba, T. Weimann, and F. J. Ahlers, Appl. Phys. Lett. **99**, 022112 (2011).

[41] J. Hu, A. F. Rigosi, M. Kruskopf, Y. Yang, B.-Y. Wu, J. Tian, A. R. Panna, H.-Y. Lee, S. U. Payagala, G. R. Jones, M. E. Kraft, D. G. Jarrett, K. Watanabe, T. Taniguchi, R. E. Elmquist, and D. B. Newell, Sci. Rep. **8**, 15018 (2018).

[42] D. A. Abanin and L. S. Levitov, Science **317**, 641 (2007).

[43] T. Lohmann, K. von Klitzing, and J. H. Smet, Nano Lett. **9**, 1973 (2009).

[44] S. T. Le, J. A. Hagmann, N. Klimov, D. B. Newell, J. U. Lee, J. Yan, and C. A. Richter (submitted).

[45] S. Matsuo, S. Takeshita, T. Tanaka, S. Nakaharai, K. Tsukagoshi, T. Moriyama, T. Ono, and K. Kobayashi, Nat. Commun. **6**, 8066 (2015).

[46] C. Kumar, M. Kuiri, and A. Das, Solid State Commun. **270**, 38 (2018).

[47] A. F. Rigosi, D. K. Patel, M. Marzano, M. Kruskopf, H. M. Hill, H. Jin, J. Hu, A. R. Hight Walker, M. Ortolano, L. Callegaro, C.-T. Liang, and D. B. Newell, Carbon **154**, 230 (2019).

[48] Commercial equipment, instruments, and materials are identified in this paper in order to specify the experimental procedure adequately. Such identification is not intended to imply recommendation or endorsement by the National Institute of Standards and Technology or the United States government, nor is it intended to imply that the materials or equipment identified are necessarily the best available for the purpose.

[49] A. F. Rigosi, D. K. Patel, M. Marzano, M. Kruskopf, H. M. Hill, H. Jin, J. Hu, R. E. Elmquist, and D. B. Newell, Physica B ∎, 411971 (2019).

[50] See www.linear.com/designtools/software/ for Linear Technology 2018 LTspice XVII.

[51] M. Ortolano and L. Callegaro, Meas. Sci. Technol. **26**, 085018 (2015).

[52] M. Kruskopf, D. M. Pakdehi, K. Pierz, S. Wundrack, R. Stosch, T. Dziomba, M. Götz, J. Baringhaus, J. Aprojanz, and C. Tegenkamp, 2D Mater. **3**, 041002 (2016).

[53] V. Panchal, Y. Yang, G. Cheng, J. Hu, M. Kruskopf, C.-I. Liu, A. F. Rigosi, C. Melios, A. R. Hight Walker, D. B. Newell, O. Kazakova, and R. E. Elmquist, Commun. Phys. **1**, 83 (2018).

[54] S. Sarkar, H. Zhang, J.-W. Huang, F. Wang, E. Bekyarova, C. N. Lau, and R. C. Haddon, Adv. Mater. **25**, 1131 (2013).

[55] J. Dai, Y. Zhao, X. Wu, X. C. Zeng, and J. Yang, J. Phys. Chem. C **117**, 22156 (2013).

[56] E. Bekyarova, S. Sarkar, S. Niyogi, M. E. Itkis, and R. C. Haddon, J. Phys. D: Appl. Phys. **45**, 154009 (2012).

[57] S. Che, K. Jasuja, S. K. Behura, P. Nguyen, T. S. Sreeprasad, and V. Berry, Nano Lett. **17**, 4381 (2017).

[58] A. F. Rigosi, M. Kruskopf, H. M. Hill, H. Jin, B.-Y. Wu, P. E. Johnson, S. Zhang, M. Berilla, A. R. Hight Walker, C. A. Hacker, D. B. Newell, and R. E. Elmquist, Carbon **142**, 468 (2019).

[59] S. Lara-Avila, K. Moth-Poulsen, R. Yakimova, T. Björnholm, V. Fal'ko, A. Tzalenchuk, and S. Kubatkin, Adv. Mater. **23**, 878 (2011).

Supplementary Material: Accessing ratios of quantized resistances in graphene *p-n* junction devices using multiple terminals

D. K. Patel,[1,2] M. Marzano,[1,3,4] C.-I Liu,[1] H. M. Hill,[1] M. Kruskopf,[1,5] H. Jin,[1,5] J. Hu,[1,5] D. B. Newell,[1] C.-T. Liang,[2] R. E. Elmquist,[1] and A. F. Rigosi[1,a)]

[1]*Physical Measurement Laboratory, National Institute of Standards and Technology (NIST), Gaithersburg, Maryland, 20899-8171, USA*

[2]*Department of Physics, National Taiwan University, Taipei, 10617, Taiwan*

[3]*Department of Electronics and Telecommunications, Politecnico di Torino, Torino, 10129, Italy*

[4]*Istituto Nazionale di Ricerca Metrologica, Torino, 10135, Italy*

[5]*Joint Quantum Institute, University of Maryland, College Park, MD 20742, USA*

Contents

1. Device fabrication and UV exposure information
2. Example calculations
3. Raman spectra for large scale homogeneity
4. Supporting AFM images

---

[a)] Author to whom correspondence should be addressed. Mail: Albert Rigosi, MS 8171, 100 Bureau Drive, NIST, Gaithersburg, MD 20899.

1.   Device fabrication and UV exposure information

Devices underwent additional fabrication steps after unmodified Hall bar devices were functionalized with $Cr(CO)_3$. The steps are listed below, with the full process illustrated in Fig. 1-SM:[∂]

1. Spin photoresist at 5000 rpm for 1 min (acceleration: 5000 rpm/s). Photoresist composed of 75 % electronic-grade propylene glycol monomethyl ether acetate, 15 % mixed cresol novolak resin, and 10 % diazo photoactive compound (sold commercially as S1813 from The Dow Chemical Company).

2. Bake chips at 115 °C for 1 min.

3. Expose to ultraviolet light (365 nm) for 5 seconds, using a photomask designed to expose only the central region of the device, as in Figure 4 (other designs shown later). Parameters were measured on a high-precision mask and bond aligner (sold commercially as the Suss MA6 from Suss Microtec). {1130 W; WEC = cont.; Vacuum mode: 10 s / 30 s / 15 s; Al-gap = 15 µm; Dosage = 100 mJ}.

4. Use solution of 97 % water, 2.3 % tetramethylammonium hydroxide, and 0.7 % polyglycol (commercially sold as MF-26A Developer from The Dow Chemical Company), for 1 min to remove exposed region.

5. Bake chips at 200 °C for 5 min.

6. Spin solution of 95 % ethyl lactate and 5 % Poly(methyl methacrylate/methacrylic acid) as a spacer layer (sold commercially as EL6 from The Dow Chemical Company). Thickness of this photoresist should be between 50 nm to 100 nm (or less). Spin rate is 5000 rpm (acceleration of 5000 rpm/s).

7. Bake chips at 170 °C for 1 min.

8. Spin photoresist at 4000 rpm for 1 min to get a desired thickness between 300 nm and 400 nm. Photoresist composed of 89 % anisole and 11 % methyl styrene / chloromethyl acrylate copolymer (sold commercially as ZEP 520A from Zeon Chemicals L. P.).

9. Bake chips at 170 °C for 1 min.

10. Expose chips to 254 nm ultraviolet light for approximately 15 hours to activate the *p*-type regions. This time can be altered based on distance from the sample.

11. Other device regions should be inherently *n*-type. Level of doping can be adjusted by annealing.

12. UV data shown in Figure 2-SM.
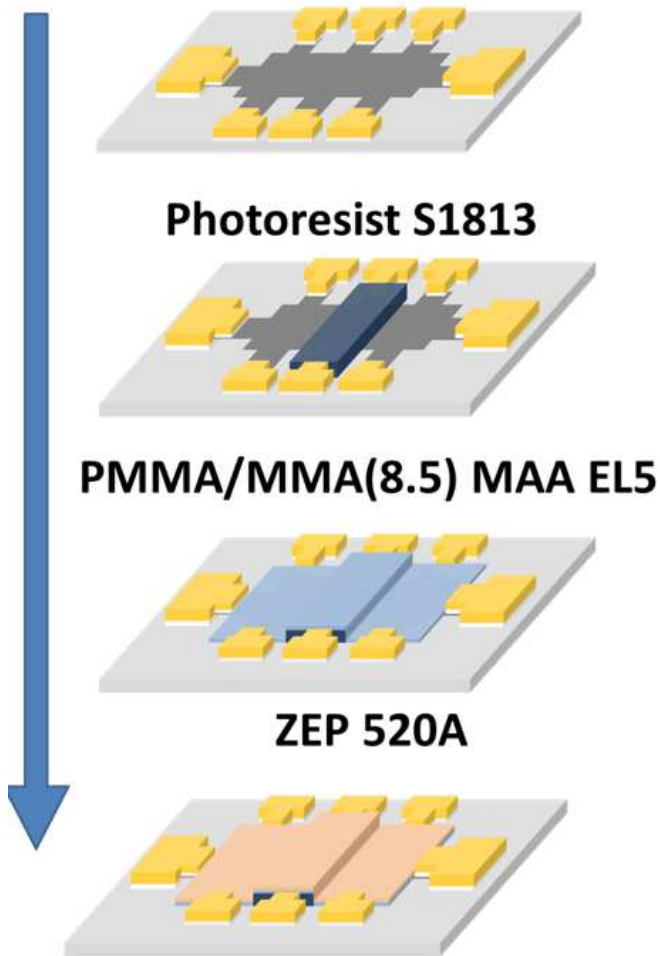
Figure 1-SM. A typical Hall bar device, after functionalization, is prepared with various polymers to enable the eventual adjustment of *p*-type and *n*-type regions.
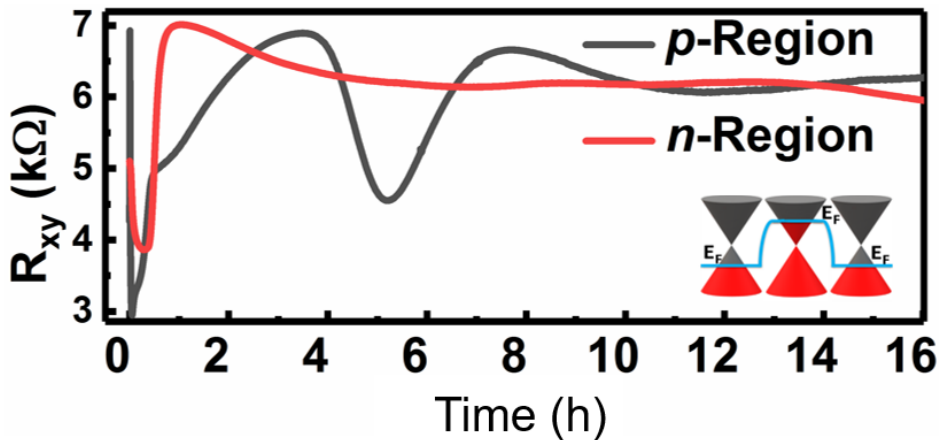
Figure 2-SM. Data of an example UV exposure session. As expected, the *n*-region, protected by a spacer layer of S1813, does not change much with time (initial transient effects aside). The *p*-region does shift after crossing the Dirac point around 7 h to 8 h. The dip at 5.5 h is the result of competing effects from the UV treatment and the device heating due to the UV bulb.

2. Example calculations

Calculations are provided below for three cases presented in the main text (Figs. 3-SM, 4-SM, 5-SM).
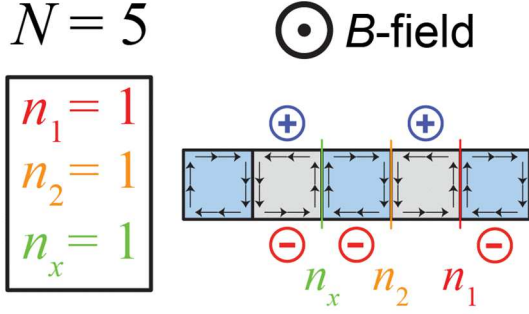
Figure 3-SM. The calculation for an example configuration from the main text is provided below. This $N = 5$ non-alternating configuration has its n_j terms assigned according to the guidelines in Ref. [1].

Once the n_j terms have been assigned, the calculation may begin. Since this is a non-alternating system, the condition of edge state cancellation along the junction marked in green in Fig. 3-SM allows us to treat the whole system as two smaller circuits in parallel. The "unit" terminal on the left gives a coefficient of effective resistance (CER) of 1. For the right branch, as described in Ref. [1], the use of the following equation is warranted:
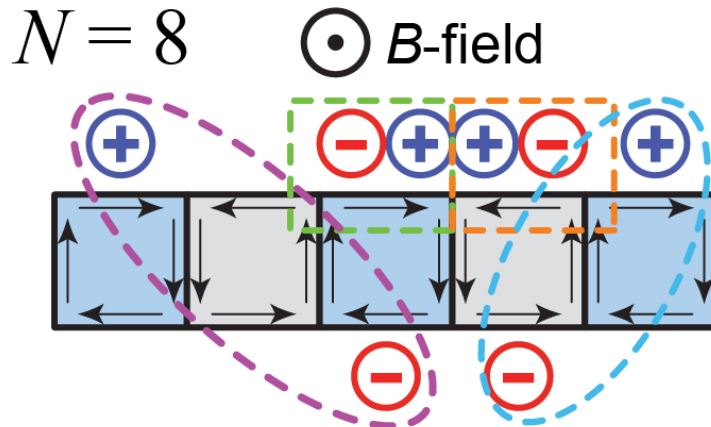
$$q_{N-1}(n_{N-1}) = \frac{q_{N-2}(n_{N-1} + 1)}{n_{N-1} + \frac{q_{N-2}}{q_{N-1}^{(0)}}}$$

(A1)

With $n_1 = 1$, we use the linear form of Eq. (A1), which is $q_2 = (n_1 + 1)$. $q_1 = 2$, and that brings us to $n_2 = 1$. If we apply the iteration in Eq. (A1) again:

$$q_2(n_2) = \frac{q_1(n_2 + 1)}{n_2 + \frac{q_1}{q_2^{(0)}}} = \frac{2(1 + 1)}{1 + \frac{2}{1}} = \frac{4}{3}$$

In the main text, the term $q_2^{(0)}$ was not directly addressed since its explanation is provided in Ref. [1]. With our two branches assigned, we can get our final CER as $\left(\frac{1}{1} + \frac{3}{4}\right)^{-1} = \frac{4}{7}$.

FIG. 4-SM. The calculation for this N = 8, non-alternating, example configuration from the main text is provided below. Dotted colored lines indicate the terminals in the various parallel circuits.

Since the next example is also a non-alternating system, the condition of edge state cancellation along various junctions allows us to demarcate four distinct parallel circuits. In Fig. 4-SM, two "unit" terminals in green and orange dotted lines give CERs of 1. The dotted blue and purple configurations are also effectively $N = 2$ systems with the purple dotted-lined system having $n_1 = 2$ and the blue dotted-lined system having $n_1 = 1$. If one sums all these branches in parallel, then the CER is:

$$\left(\frac{1}{1} + \frac{1}{1} + \frac{1}{3} + \frac{1}{2}\right)^{-1} = \frac{6}{17}.$$
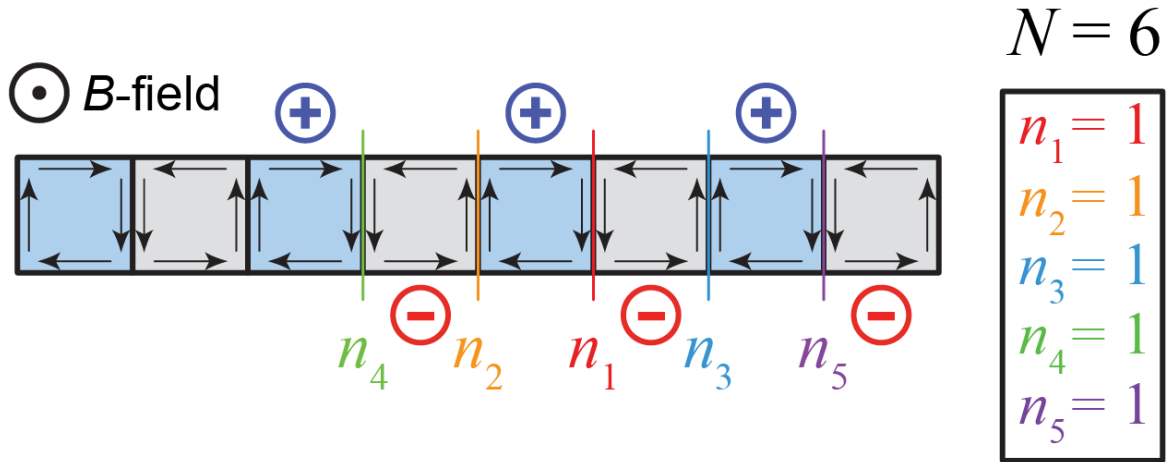

FIG. 5-SM. The calculation for this $N = 6$ alternating configuration from the main text is provided below. The n_j terms have been assigned according to the guidelines in Ref. [1].

This calculation will be the most involved of the examples. After the n_j terms have been assigned according to the guidelines in Ref. [1], one can begin using Eq. (A1) to begin the iterative algorithm. Since $n_1 = 1$, one obtains $q_2 = (n_1 + 1) = 2$. Next, with $n_2 = 1$:

$$q_2(n_2) = \frac{q_1(n_2 + 1)}{n_2 + \frac{q_1}{q_2^{(0)}}} = \frac{2(1 + 1)}{1 + \frac{2}{1}} = \frac{4}{3}$$

Then, with $n_3 = 1$, approaching the next iteration to get q_3 (see Fig. 6-SM) becomes slightly more difficult since the term $q_3^{(0)}$ needs evaluation.
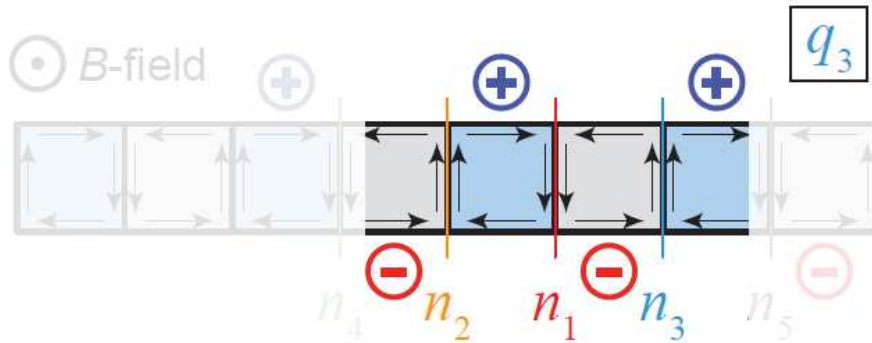
FIG. 6-SM. For subsequent iterations of the calculation for the configuration in Fig. 5-SM, one must focus on smaller subset configurations to determine q_5 mathematically. Here, q_3 is dependent on the term $q_3^{(0)}$, which is the CER for the limiting case where $n_3 = 0$ (see Fig. 7-SM).

5
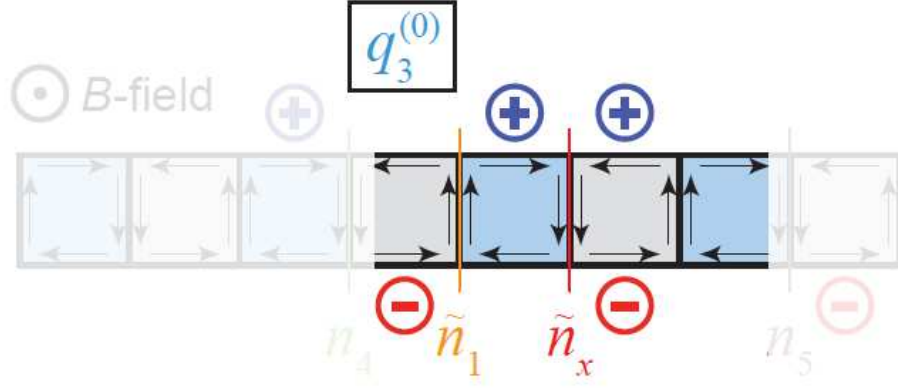
FIG. 7-SM. Evaluation for $q_3^{(0)}$ is easier to accomplish with this visual guide. For the limiting case where $n_3 = 0$ (where n_3 is defined in Fig. 6-SM), a "new" configuration must be evaluated. New parameters have been labeled in orange and red. This configuration contains a unit terminal on the right that is isolated from the left branch defined by the parameter $\tilde{n}_1$. Therefore, $q_3^{(0)} = \left(\frac{1}{1} + \frac{1}{2}\right)^{-1} = \frac{2}{3}$.

From Fig. 7-SM, we get $q_3^{(0)} = \frac{2}{3}$ since the first parallel branch (unit terminal on right) gives a CER of 1 and the left parallel branch gives a CER of 2. This allows us to get q_3:

$$q_3(n_3) = \frac{q_2(n_3 + 1)}{n_3 + \frac{q_2}{q_3^{(0)}}} = \frac{\frac{4}{3}(1 + 1)}{1 + \frac{4/3}{2/3}} = \frac{8}{9}$$

The next iteration continues with q_4, where we evaluate the CER of the entire circuit shown in Fig. 8-SM.
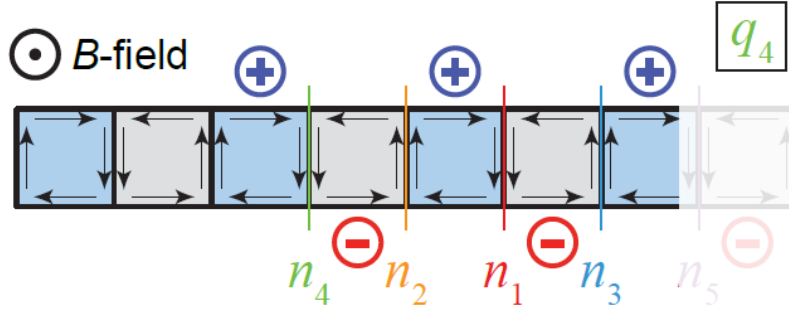
FIG. 8-SM. Evaluation continues with q_4, where this five-terminal configuration must be solved before continuing. The formula contains the term $q_4^{(0)}$, which must first be evaluated before q_4 can be solved.
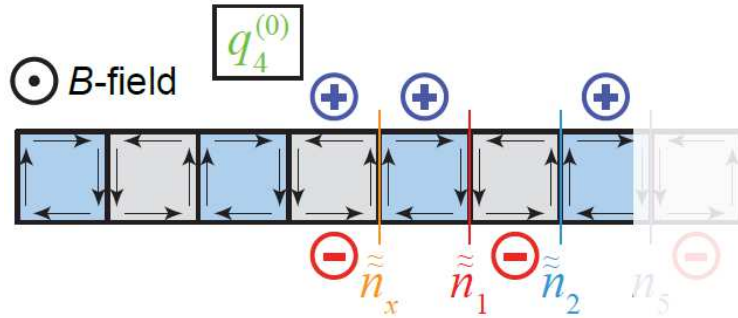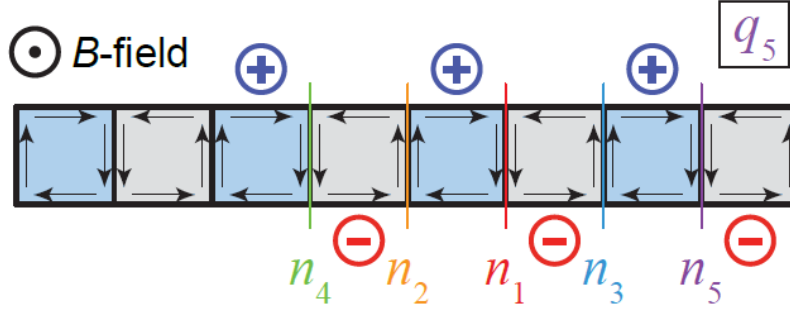

FIG. 9-SM. Evaluation for $q_4^{(0)}$ requires $n_4 = 0$ (where n_4 is defined in Fig. 8-SM), giving us a "new" configuration to solve here. This configuration contains a unit terminal on the left that is isolated from the right branch defined by the parameters (\double-tilde) n_1 and n_2.

6

In Fig. 9-SM, $q_4^{(0)} = \frac{4}{7}$ since it is numerically identical to Fig. 3-SM. This allows us to get q_4:

$$q_4(n_4) = \frac{q_3(n_4 + 1)}{n_4 + \frac{q_3}{q_4^{(0)}}} = \frac{\frac{8}{9}(1 + 1)}{1 + \frac{8/9}{4/7}} = \frac{16}{23}$$

The final iteration ends with q_5, where we evaluate the CER of the entire circuit shown in Fig. 10-SM.

FIG. 10-SM. Evaluation ends with q_5, where this six-terminal configuration must be solved for the final answer. The formula contains the term $q_5^{(0)}$, which must first be evaluated before q_5 can be solved.
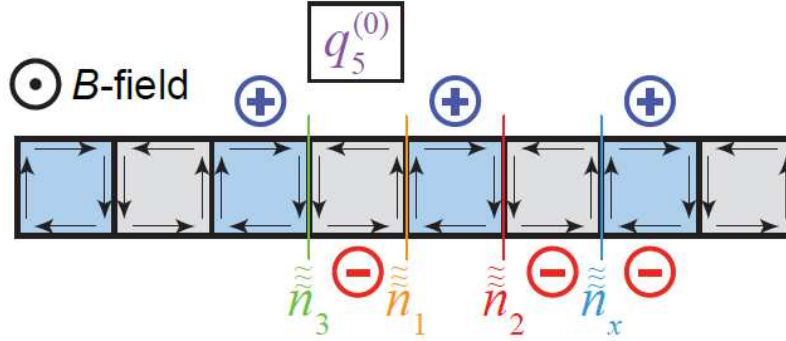
FIG. 11-SM. Evaluation for $q_5^{(0)}$ requires $n_5 = 0$ (where n_5 is defined in Fig. 10-SM), giving us a "new" configuration to solve here. This configuration contains a unit terminal on the far right that is isolated from the right branch defined by the parameters (\triple-tilde) n_1, n_2, and n_3.

In Fig. 11-SM, $q_5^{(0)}$ is relatively straightforward since there are only two parallel branches: a unit terminal giving a CER of 1 and an alternating four-terminal configuration that is mathematically identical to q_3, whose CER is $\frac{8}{9}$. This allows us to get $q_5^{(0)}$: $q_5^{(0)} = \left(\frac{1}{1} + \frac{9}{8}\right)^{-1} = \frac{8}{17}$

$$q_5(n_5) = \frac{q_4(n_5 + 1)}{n_5 + \frac{q_4}{q_5^{(0)}}} = \frac{\frac{16}{23}(1 + 1)}{1 + \frac{16/23}{8/17}} = \frac{32}{57}$$

The final result is $q_5 = \frac{32}{57}$, and is closely matched by the experimental data in the main text.

3. Raman spectra for large scale homogeneity

In Fig. 12-SM, a Raman map was acquired with a Renishaw InVia micro-Raman spectrometer[see notes] using a 633 nm wavelength excitation laser source and a backscattering configuration. The spot size was about 1 μm, the acquisition times were 300 s, the laser power was 1.7 mW power, and the optical path included a 50 × objective and 1200 mm^{-1} grating. The spread is indicative of a relatively homogeneous sample.
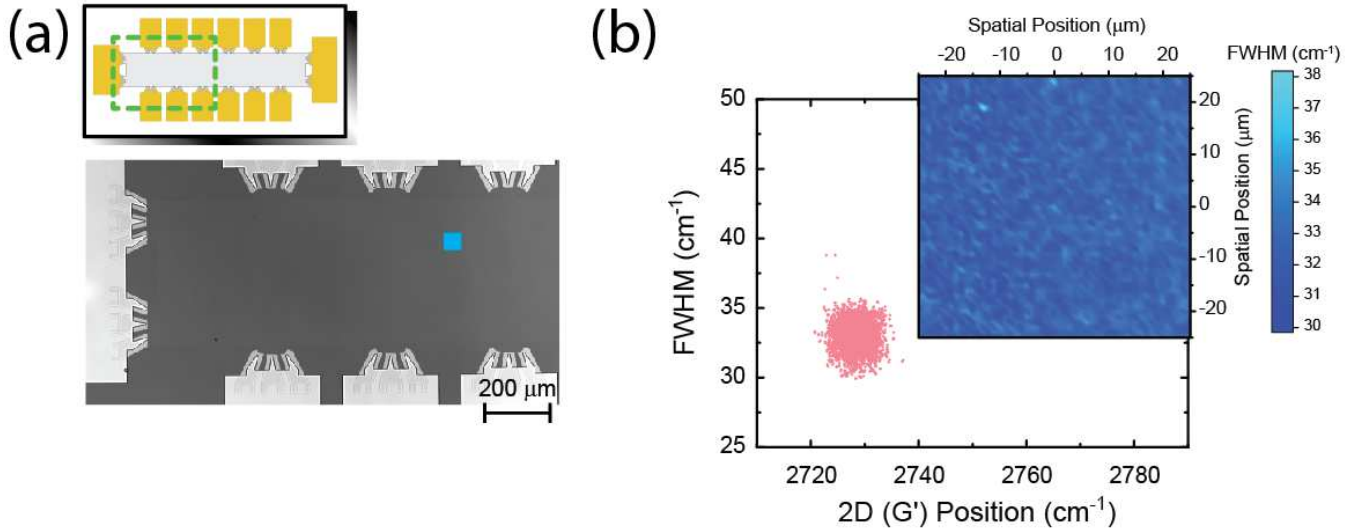

FIG. 12-SM. (a) Optical image of example device after growth. (b) A Raman map was acquired to ensure sample homogeneity. The map was taken over the area shaded in light blue in (a).

4. Supporting AFM images

Prior to deposition of $Cr(CO)_3$ and the various polymers required for large-scale electron density modulation, AFM images were acquired on post-growth graphene areas to verify homogeneity. The polymer-assisted growth suppressed the formation of nanoscopic steps typically seen in SiC sublimation.
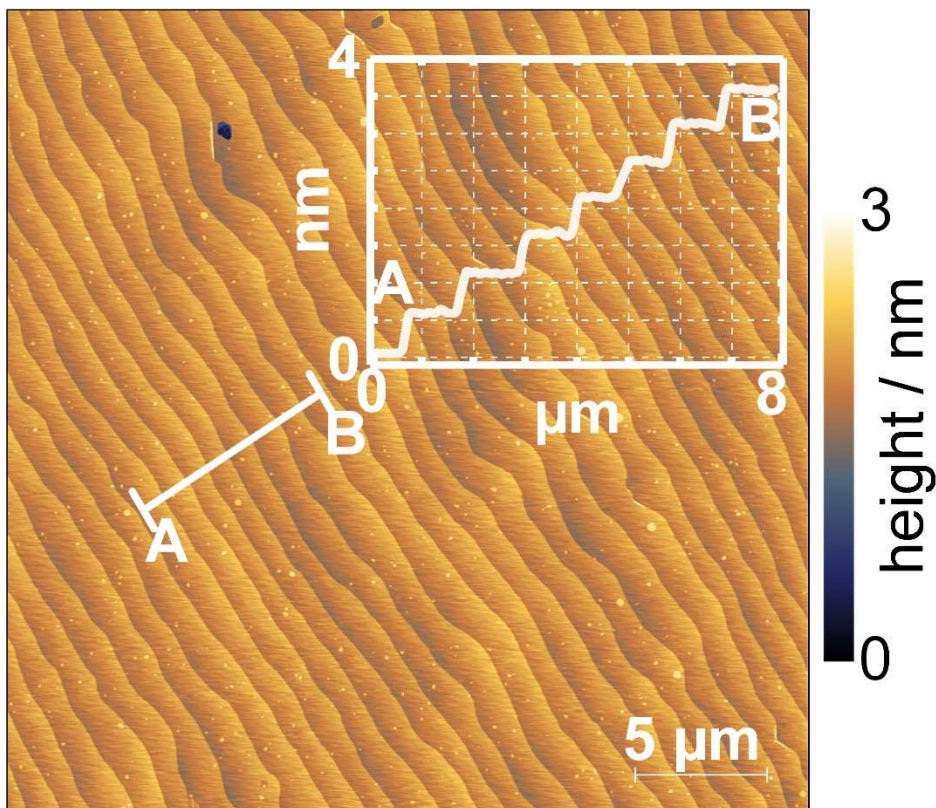
FIG. 13-SM. Example AFM image for approximate region of the device similar to Raman map and taken prior to functionalization. This image verifies the suppression of overactive step bunching typically seen with SiC sublimation. Aside from several spot contaminants, the graphene can grow unimpeded along the ordered steps.

NOTES

[a] *Commercial equipment, instruments, and materials are identified in this paper in order to specify the experimental procedure adequately. Such identification is not intended to imply recommendation or endorsement by the National Institute of Standards and Technology or the United States government, nor is it intended to imply that the materials or equipment identified are necessarily the best available for the purpose.*

REFERENCES

[1]A.F. Rigosi, D.K. Patel, M. Marzano, M. Kruskopf, H.M. Hill, H. Jin, J. Hu, A.R. Hight Walker, and D.B. Newell, Physica B, **DOI:** 10.1016/j.physb.2019.411971 (2019).